IEEE Access
Multidisciplinary ⋮ Rapid Review ⋮ Open Access Journal

Received 9 September 2026, accepted 1 October 2026, date of publication 8 October 2026, date of current version 14 October 2026.

Digital Object Identifier 10.1109/ACCESS.2026.3741708

RESEARCH ARTICLE

CMA-Assisted Wideband Vivaldi Antenna for UAV-Based Distributed Beamforming in EW/ISR Applications

MYEONG-JUN KANG[1,*], SEONGKWON YOON[2,*], JUN-HYEON KANG[3], SEYEON LEE[3], JEAHOON CHO[3], AND SUNWOO KIM[3], (Senior Member, IEEE)

[1]Hanwha Systems, Seongnam-si, Gyeonggi-do 13488, South Korea
[2]Agency for Defense Development (ADD), Daejeon 34186, South Korea
[3]Beyond-G Global Innovation Center, Hanyang University, Seoul 04763, South Korea

Corresponding author: Sunwoo Kim (remero@hanyang.ac.kr)

This work was supported in part by the National Research Foundation of Korea (NRF) grant funded by Korean Government [Ministry of Science and ICT (MSIT)] under Grant NRF-2023R1A2C3002890 and Grant RS-2024-00409492.

*Myeong-Jun Kang and Seongkwon Yoon are co-first authors.

ABSTRACT A CMA-assisted compact wideband antipodal Vivaldi antenna is proposed for UAV-based intelligence, surveillance, and reconnaissance (ISR) and electronic warfare (EW) applications. The antenna operates from 0.4 to 7.3 GHz, achieving an ultra-wide fractional bandwidth of 179% with a compact electrical size. During the initial design stage, unstable end-fire radiation is observed around 0.8 GHz, a critical band for long-range ISR and EW operations. To address this issue, characteristic mode analysis (CMA) is employed to identify the dominant radiation mechanism and suppress undesired broadside modes. Based on the CMA results, a wing-shaped resonator is introduced to stabilize end-fire radiation at low frequencies. In addition, a stepped feeding structure is incorporated to improve impedance matching across the operating band, enabling ultra-wideband performance without using bulky dielectric loading or multilayer structures. The proposed antenna achieves a maximum realized gain of 9.6 dBi. Platform-level feasibility is evaluated by integrating the antenna with a quadrotor unmanned aerial vehicle (UAV) using a hybrid electromagnetic simulation framework. The system-level impact of the embedded element pattern is further investigated at 0.8 and 2.4 GHz through distributed beamforming simulations against an isotropic baseline. The Vivaldi manifold provides a 9.8 dB signal-to-interference-plus-noise ratio (SINR) improvement over the isotropic beamformer baseline at 0.8 GHz and maintains positive signal-to-clutter-plus-noise ratio (SCNR) for all beamformers at 2.4 GHz, where the isotropic baseline degrades to −3.51 dB. These results show that the embedded directivity acts as a manifold-shaping spatial pre-filter that suppresses wide-angle leakage in electrically sparse distributed UAV formations.

INDEX TERMS Beamforming, characteristic mode analysis, electronic warfare, Vivaldi antenna, wideband.

I. INTRODUCTION

The electromagnetic spectrum (EMS) has become a critical domain in modern military operations due to the rapid proliferation of wireless communication systems, multifunctional radars, and autonomous sensing platforms. Electronic warfare (EW) aims to exploit and control the EMS by detecting, intercepting, and disrupting adversarial electromagnetic emissions [1], while intelligence, surveillance, and reconnaissance (ISR) systems rely on wideband sensing to enhance situational awareness. As the operational environment becomes increasingly congested and contested, EW and ISR platforms are required to operate over wide frequency ranges with high sensitivity, directional selectivity, and rapid response capabilities [2], [3].

Unmanned aerial vehicles (UAVs) have recently emerged as key platforms for EW and ISR missions owing to their mobility, flexibility, and reduced operational risk compared

The associate editor coordinating the review of this manuscript and approving it for publication was Bilal A. Khawaja.

© 2026 The Authors. This work is licensed under a Creative Commons Attribution 4.0 License.
For more information, see https://creativecommons.org/licenses/by/4.0/

to manned systems [3], [4]. Beyond standalone deployment, multiple UAVs can be cooperatively utilized as a distributed aerial sensing aperture, enabling spatially distributed receive beamforming for directional signal collection, emitter localization, and interference suppression over a wide area [5], [6], [7]. In such distributed systems, the overall sensing performance is governed not only by array geometry but also by the embedded radiation characteristics of each individual antenna element.

However, most existing antenna designs are evaluated solely in free space, neglecting platform-induced scattering and radiation pattern distortion [8], [9]. This limitation becomes particularly critical in UAV-based distributed sensing systems, where beamforming performance depends on the embedded element patterns rather than idealized antenna responses [3], [10]. Consequently, ignoring platform effects may lead to significant degradation in directional selectivity, interference suppression capability, and overall sensing performance. Therefore, antenna designs intended for UAV-based applications must be validated within realistic platform-integrated environments [6], [7].

In distributed UAV-based sensing systems, beamforming performance is typically improved through advanced digital signal processing techniques such as adaptive beamforming and multi-objective optimization. However, these approaches implicitly assume ideal or isotropic antenna elements, thereby neglecting the impact of the embedded element radiation characteristics. Recent distributed UAV beamforming studies, including learning-based and optimization-based designs as well as experimental demonstrations, likewise represent the array response with phase-only steering vectors [6], [11], [12], [13]. In practice, the antenna response acts as a spatial pre-filter that directly shapes the array manifold, influencing sidelobe levels, interference suppression capability, and overall beamforming performance.

Therefore, the design of antenna elements should not be considered independently from the beamforming process. Instead, antenna characteristics and beamforming performance must be jointly considered, particularly in distributed UAV scenarios where platform-induced distortions further complicate the array response.

Low-profile bow-tie and dielectric resonator radiators and pattern-reconfigurable arrays also achieve wideband operation with beam-shaping capability, but a forward-looking EW payload requires a fixed end-fire beam maintained across the entire band without active control [14], [15]. Among various broadband antennas, Vivaldi antennas have attracted significant attention due to their inherent ultra-wideband characteristics, end-fire radiation, and structural simplicity [16], [17]. These properties make them well-suited for UAV-based ISR and EW applications requiring wideband directional coverage [9], [18], [19], [20]. Nevertheless, achieving stable end-fire radiation over a wide frequency range remains a fundamental challenge, particularly at low frequencies. In this region, Vivaldi antennas often exhibit undesired broadside radiation due to dominant current modes, which directly degrades forward-looking sensing capability.

Existing approaches to address this issue typically rely on empirical geometry modifications such as nonuniform tapering [21], slot loading [22], [23], [24], [25], or dielectric and metamaterial loading [26], [27]. While these methods can improve impedance matching or bandwidth, they often increase structural complexity and do not explicitly control the underlying radiation mechanisms. As a result, the relationship between antenna geometry and radiation behavior remains insufficiently understood, leading to suboptimal performance, especially in the low-frequency region.

To overcome these limitations, this work proposes a characteristic mode analysis (CMA)-driven design framework for a compact wideband antipodal Vivaldi antenna. Unlike conventional geometry-driven approaches, CMA provides a physics-based methodology to identify and control dominant radiation modes [28], [29], [30], [31], [32]. In particular, the unstable radiation behavior observed at 0.8 GHz is analyzed through CMA, revealing that a dominant broadside mode governs the radiation response. Based on this insight, a wing-shaped resonator is introduced to suppress the undesired mode and promote stable end-fire radiation by reshaping the surface current distribution along the antenna aperture.

In addition, a stepped feeding structure is employed to improve impedance matching across the entire operating band, enabling ultra-wideband performance from 0.4 to 7.3 GHz without relying on bulky loading structures or multilayer configurations. The proposed antenna achieves stable end-fire radiation over representative ISR/EW frequency bands, along with a maximum realized gain of 9.6 dBi.

Furthermore, to bridge the gap between idealized antenna design and practical deployment, the proposed antenna is integrated with a representative UAV platform (Tarot X4) and analyzed through hybrid full-wave electromagnetic simulation, thereby capturing platform-induced scattering effects on the embedded element patterns. The practical utility of the proposed design is then demonstrated through distributed beamforming simulations in a multi-UAV scenario, where its performance is compared against an ideal isotropic baseline in terms of directional signal collection and interference suppression.

This work makes the following key contributions:

1) A CMA-driven design framework is proposed to enable physics-based control of radiation modes for stabilizing low-frequency end-fire radiation in Vivaldi antennas.
2) The proposed antenna is evaluated by full-wave simulation in a UAV-integrated environment, explicitly accounting for platform-induced scattering and embedded element pattern distortion.
3) The impact of the antenna on distributed beamforming performance is demonstrated, showing that the proposed design effectively improves directional signal collection and interference suppression compared to an ideal isotropic baseline.

The remainder of this paper is organized as follows. Section II presents the CMA-based design methodology and radiation mechanism analysis of the proposed antenna. Section III introduces the distributed UAV beamforming framework. Section IV describes the fabrication and measurement results. Section V investigates the UAV-integrated antenna performance through full-wave simulations. Section VI presents the beamforming performance evaluation. Finally, concluding remarks are provided in Section VII.

II. CMA-ASSISTED DESIGN OF AN ANTIPODAL VIVALDI ANTENNA

A. INITIAL ANTIPODAL VIVALDI ANTENNA CONFIGURATION

The overall geometry and performance evolution of the proposed antenna are summarized in Fig. 1 and Fig. 2, respectively. The design begins with the initial antipodal Vivaldi antenna (Antenna I), followed by the introduction of a wing-shaped resonator and a stepped feeding structure to improve the radiation characteristics and impedance matching. All geometrical parameters of the proposed antenna are summarized in Table 1. Together with the taper coefficients a and a_1 of (1) and (2) and the rotation angle Rot_C of the elliptical slots, these values completely specify the aperture profile, the wing-shaped resonator, and the stepped feeding structure labeled in Fig. 1, so that the geometry can be reproduced without further information.

As shown in Fig. 1(a), the overall size of the antenna is $190\times200\times2.4\,\text{mm}^3$, which corresponds to $0.25\lambda_0\times0.27\lambda_0\times0.0032\lambda_0$, where λ_0 denotes the free-space wavelength at the lowest operating frequency of 0.4 GHz. The antenna is designed on an FR-4 substrate with a relative permittivity of $\varepsilon_r = 4.4$ and a loss tangent of $\tan\delta = 0.025$.

The radiating aperture of Antenna I is defined by an exponential taper curve (C_1), as expressed in (1).

$$C_1:\ W_{TL} + (W_V - W_{TL}) \times \frac{e^{at} - 1}{e^{a} - 1}, \quad 0 \le t \le 1 \qquad (1)$$

The exponential profile provides a smooth and continuous variation of the slot width along the propagation direction, which facilitates broadband operation by supporting multiple resonant modes over a wide frequency range. By gradually modifying the effective electrical length of the aperture, the exponential taper enables the excitation of multiple resonant modes, thereby contributing to ultra-wideband radiation characteristics.

In addition, the lower edge of the radiator is shaped with an elliptical cut to improve current distribution and radiation behavior in the low-frequency region. The ground plane, which acts as a reflector for forming end-fire radiation, is also designed using an exponential taper curve (C_2), as described in (2).

$$C_2:\ L_{GS} + (L_G - L_{GS}) \times \frac{e^{a_1 t} - 1}{e^{a_1} - 1}, \quad 0 \le t \le 1 \qquad (2)$$

By employing the exponential profile for the ground structure, the effective electrical length of the reflector is smoothly varied along the propagation direction, enabling multi-resonant behavior and contributing to broadband radiation characteristics.

TABLE 1. Optimized geometrical parameters of the proposed antenna.

Parameter	Value (mm)	Parameter	Value (mm)
W_S	200	L_S	190
W_V	19	L_V	160
L_G	10	L_{GS}	5
R_x	100	R_y	20
R_{x1}	40	R_{y1}	5
G_S	25	W_{TL}	2.8
W_F	4.25	L_F	10
G_F	2	Rot_C	40°
a	2.5	a_1	3

For the initial antenna (Antenna I), multiple resonances are formed across the operating band owing to the exponential taper profiles. Although these resonances contribute to broadband behavior, impedance matching in the mid-frequency region is not yet fully optimized at this stage, as shown in Fig. 2(a). The corresponding simulated radiation patterns are presented in Fig. 2(b)–(e). As observed in Fig. 2(b), the radiation pattern at 0.8 GHz exhibits dominant broadside radiation rather than the desired end-fire behavior. In contrast, clear end-fire radiation characteristics are observed at higher frequencies, as shown in Fig. 2(c)–(e).

To investigate the underlying radiation mechanism responsible for the degraded end-fire performance at 0.8 GHz, CMA is conducted in the following subsection. Based on the modal analysis, an elliptical-slot structure is introduced to suppress the dominant broadside radiation mode and improve the radiation characteristics in the lower-frequency region.

B. CHARACTERISTIC MODE ANALYSIS FOR END-FIRE RADIATION MECHANISM

CMA is an eigenmode-based technique that provides physical insight into the radiation behavior of conducting structures by decomposing the induced surface currents into a set of orthogonal characteristic modes [33]. These modes are determined solely by the geometry and material properties of the structure and are independent of external excitation sources. Consequently, CMA enables systematic investigation of the inherent resonant mechanisms of an antenna and provides a powerful theoretical framework for antenna design and optimization [34], [35], [36].

For a perfectly conducting structure, the surface current distribution $\mathbf{J}$ can be expressed as a linear superposition of characteristic mode currents $\mathbf{J}_n$ as

$$\mathbf{J} = \sum_n a_n \mathbf{J}_n, \qquad (3)$$

where a_n denotes the complex modal weighting coefficient (MWC) of the nth characteristic mode.

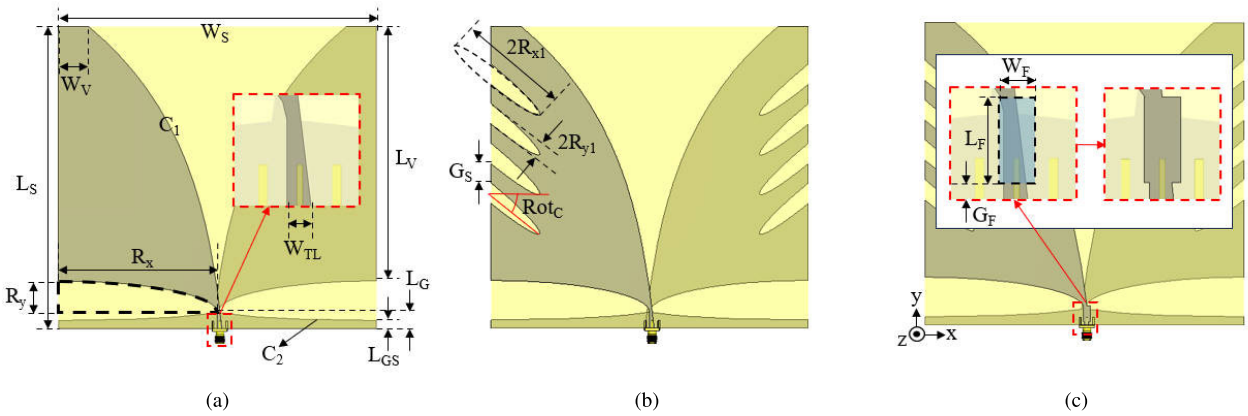


FIGURE 1. Geometry evolution of the proposed antenna: (a) Antenna I, the initial antipodal Vivaldi antenna; (b) Antenna II with the wing-shaped resonator; (c) Antenna III with the stepped feeding structure.

The contribution of each characteristic mode under a given excitation can be evaluated using the MWC, expressed as

$$a_n = \frac{\langle \mathbf{E}^i_{\tan}, \mathbf{J}_n \rangle}{1 + j\lambda_n}, \tag{4}$$

where $\mathbf{E}^i_{\tan}$ denotes the incident tangential electric field and $\langle \cdot, \cdot \rangle$ represents the inner product. The MWC indicates how strongly a particular mode is excited by the feeding structure.

In addition, the resonant behavior of each characteristic mode is quantified by the modal significance (MS), defined as

$$\mathrm{MS}_n = \left| \frac{1}{1 + j\lambda_n} \right|. \tag{5}$$

The MS value ranges from 0 to 1, where $\mathrm{MS}_n = 1$ indicates that the corresponding mode is at resonance. In practical antenna analysis, a characteristic mode is generally regarded as radiative and physically significant when its MS exceeds 0.707, corresponding to the half-power point of the resonant response. Since the MS is an intrinsic property of the structure, it provides a clear indication of which modes dominate radiation at a given frequency.

Based on the theoretical background of CMA described above, the characteristic modes of the initial antipodal Vivaldi antenna are investigated to clarify the radiation mechanism responsible for the degraded end-fire performance around 0.8 GHz. Dashed lines in Fig. 4(a) and (b) show the MS and MWC of the first three characteristic modes, respectively. As observed from the MS curves, Mode 1 to Mode 3 are the dominant modes within the band of interest, and both Mode 2 and Mode 3 exhibit relatively high MS values around 0.8 GHz. However, as indicated by the MWC results in Fig. 4(b), Mode 3 is weakly excited at 0.8 GHz and contributes negligibly to radiation. Consequently, Mode 2 becomes the dominant radiating mode in this frequency region.

To further investigate the radiation behavior of each characteristic mode, Fig. 5 presents the surface current distributions and corresponding radiation patterns. Fig. 5(a) and (b) show the current distribution and radiation pattern of Mode 1, respectively, while Fig. 5(c) and (d) illustrate the corresponding results of Mode 2. Fig. 5(e) and (f) present the current distribution and radiation pattern of Mode 3, respectively. As shown in Fig. 5(d), Mode 2 exhibits a broadside radiation pattern rather than the desired end-fire behavior. This can be attributed to the surface current distribution in Fig. 5(c), where the dominant currents are oriented along the vertical direction of the aperture. As a result, the radiated fields are predominantly formed in the direction perpendicular to the current flow, leading to a broadside radiation pattern.

To modify the current orientation and promote end-fire radiation, an elliptical-slot structure is introduced symmetrically on both sides of the radiator, forming a wing-shaped resonator, as illustrated in Fig. 1(b). The proposed slot structure is designed to redistribute the surface currents along the longitudinal direction of the aperture, thereby favoring end-fire radiation. To verify the impact of the wing-shaped resonator on the modal behavior, CMA is performed again for the modified structure.

Solid lines in Fig. 4(a) and (b) show the MS and MWC results of the proposed wing-shaped resonator, respectively. Compared with the initial antenna, the modified structure exhibits a clear change in modal behavior around 0.8 GHz, indicating that the proposed slot structure effectively alters the dominant radiation mechanism.

To further examine the radiation characteristics of the modified structure, Fig. 6 presents the surface current distributions and corresponding radiation patterns of the first three characteristic modes. Fig. 6(a) and (b) show the current distribution and radiation pattern of Mode 1, respectively, while Fig. 6(c) and (d) illustrate the corresponding results of Mode 2. Fig. 6(e) and (f) present the current distribution and radiation pattern of Mode 3, respectively. As clearly observed in Fig. 6(d), the dominant radiation mode exhibits a stable end-fire radiation pattern. This improvement is attributed to the modified surface current distribution shown in Fig. 6(c), where the dominant current is redirected along the longitudinal axis of the antenna. As a result, the proposed

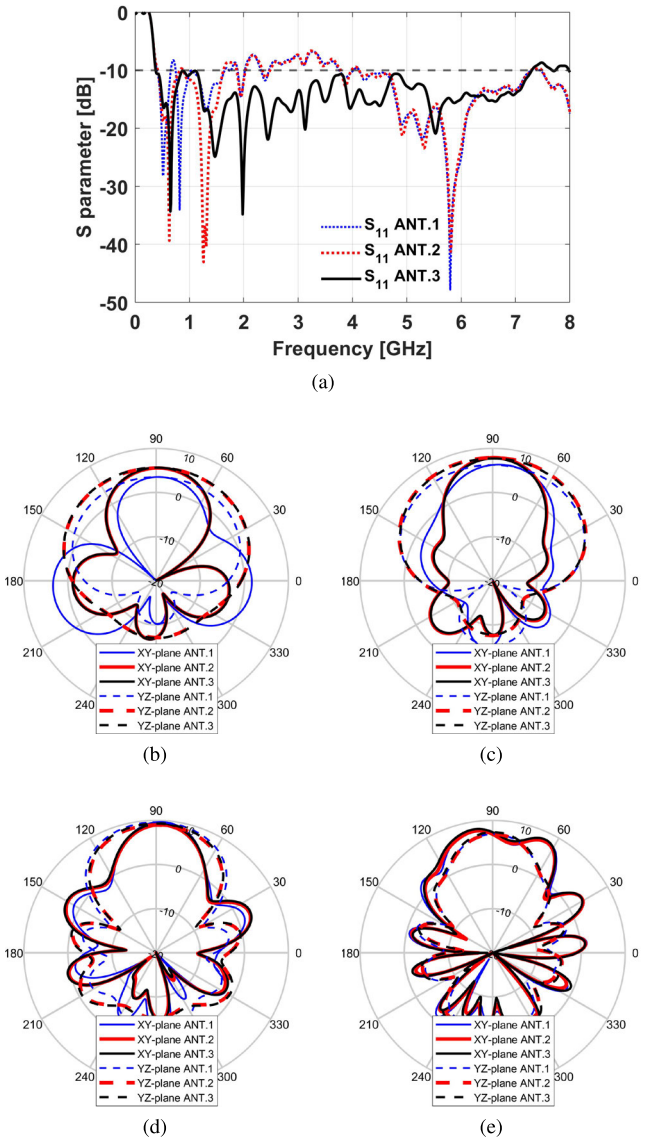


FIGURE 2. Performance evolution of the proposed antenna: (a) simulated reflection coefficients of Antenna I–III, and simulated radiation patterns at (b) 0.8 GHz, (c) 1.2 GHz, (d) 2.4 GHz, and (e) 5.8 GHz. For the radiation patterns, solid and dashed lines denote the XY- and YZ-plane results, respectively.

wing-shaped resonator effectively suppresses the undesired broadside radiation mode and enhances the dominant end-fire radiation mode in the lower-frequency region.

The corresponding results of full-wave simulation are indicated by the red line in Fig. 2. As shown in Fig. 2(a), the introduction of the wing-shaped resonator improves the impedance matching in the lower-frequency region compared with the initial antenna. In particular, Fig. 2(b) demonstrates that the broadside radiation observed in the initial antenna at 0.8 GHz is successfully transformed into the desired end-fire radiation. In contrast, the radiation patterns at higher frequencies, shown in Fig. 2(c)–(e), remain largely unchanged, indicating that the proposed structure primarily

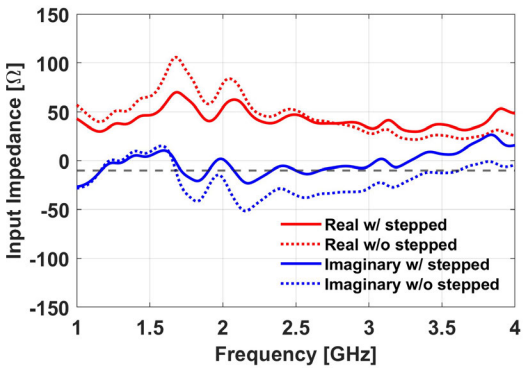


FIGURE 3. Input impedance of the proposed antenna with and without the stepped feeding structure.

improves the low-frequency radiation behavior without significantly affecting the higher-frequency characteristics.

Although the radiation characteristics are effectively improved through the proposed resonator structure, further optimization is still required to achieve broadband impedance matching over the entire operating band. Therefore, in the following subsection, a stepped feeding structure is introduced to provide a smooth impedance transition between the feed line and the radiating aperture.

C. STEPPED FEEDING STRUCTURE FOR BROADBAND IMPEDANCE MATCHING

To further improve the bandwidth, the feeding region is modified by introducing a rectangular stepped structure that functions as a multi-stage impedance transformer between the microstrip feed line and the tapered slot aperture. This configuration provides a gradual impedance transition and suppresses abrupt impedance discontinuities near the feed region.

For clarity, Fig. 3 presents the input impedance in the 1–4 GHz range, where impedance matching is most challenging. The real and imaginary parts of the input impedance with and without the stepped feeding structure are compared. With the stepped feed, the real part remains close to 50 Ω while the variation of the reactance is significantly reduced, indicating improved impedance transition behavior. The corresponding results are indicated by the black line in Fig. 2. The reflection coefficient is shown in Fig. 2(a), which confirms that the impedance matching in the lower-frequency region is noticeably improved. As a result, the proposed antenna achieves an ultra-wide operating band from 0.4 GHz to 7.3 GHz (FBW: 179%). It can be observed, as shown in Figs. 2(b)–(e), that the stepped feeding structure does not significantly affect the radiation characteristics, and the desired end-fire radiation behavior is maintained over the representative frequencies.

Based on the antenna design established above, the UAV-based distributed beamforming methodology is introduced in the following section.

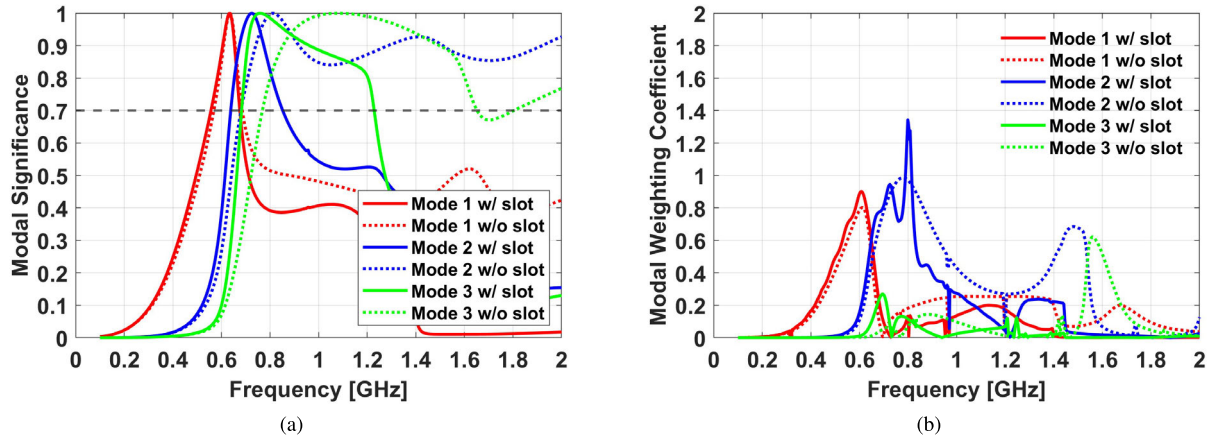


FIGURE 4. CMA results of the proposed wing-shaped resonator: (a) MS and (b) MWC.

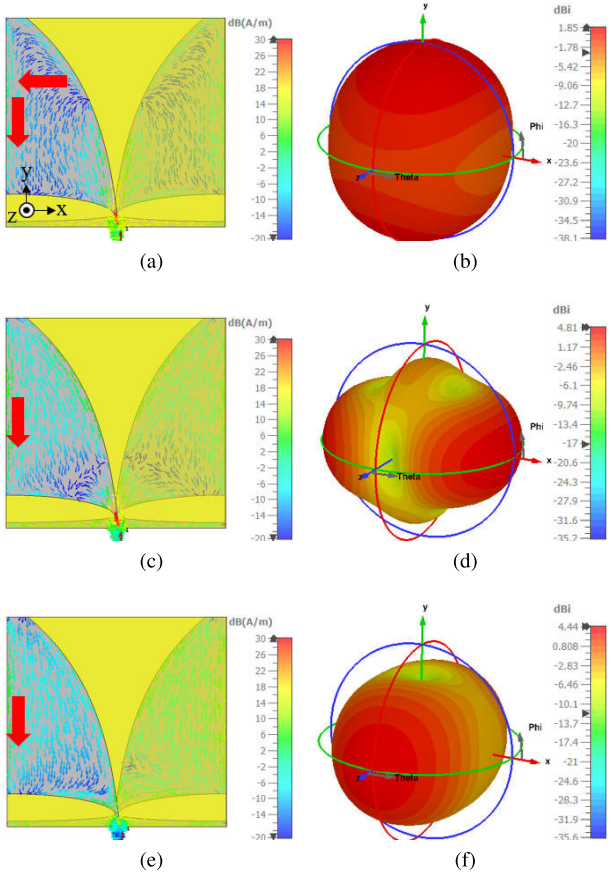


FIGURE 5. CMA results of the initial antipodal Vivaldi antenna: (a) Mode 1 current distribution, (b) Mode 1 radiation pattern, (c) Mode 2 current distribution, (d) Mode 2 radiation pattern, (e) Mode 3 current distribution, and (f) Mode 3 radiation pattern.

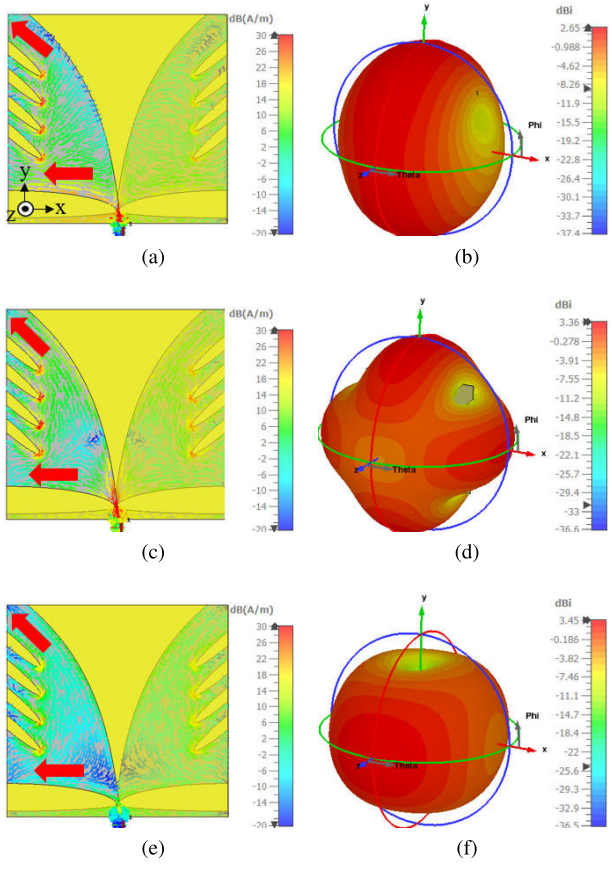


FIGURE 6. CMA results of the proposed wing-shaped resonator: (a) Mode 1 current distribution, (b) Mode 1 radiation pattern, (c) Mode 2 current distribution, (d) Mode 2 radiation pattern, (e) Mode 3 current distribution, and (f) Mode 3 radiation pattern.

III. DISTRIBUTED UAV BEAMFORMING METHODOLOGY

A. DISTRIBUTED SWARM GEOMETRY AND EMBEDDED ELEMENT MANIFOLD

To evaluate cooperative sensing under realistic platform effects, we consider a six-UAV swarm in which each UAV carries two antenna elements, yielding a total of $M = 12$ elements. The swarm is deployed in a six-node uniform circular array (UCA) formation, as shown in Fig. 7. Each UAV has two closely spaced elements with an inter-element spacing of $\lambda/2$ at 5.8 GHz, which is the highest frequency among the frequencies of interest, corresponding to 25.86 mm and

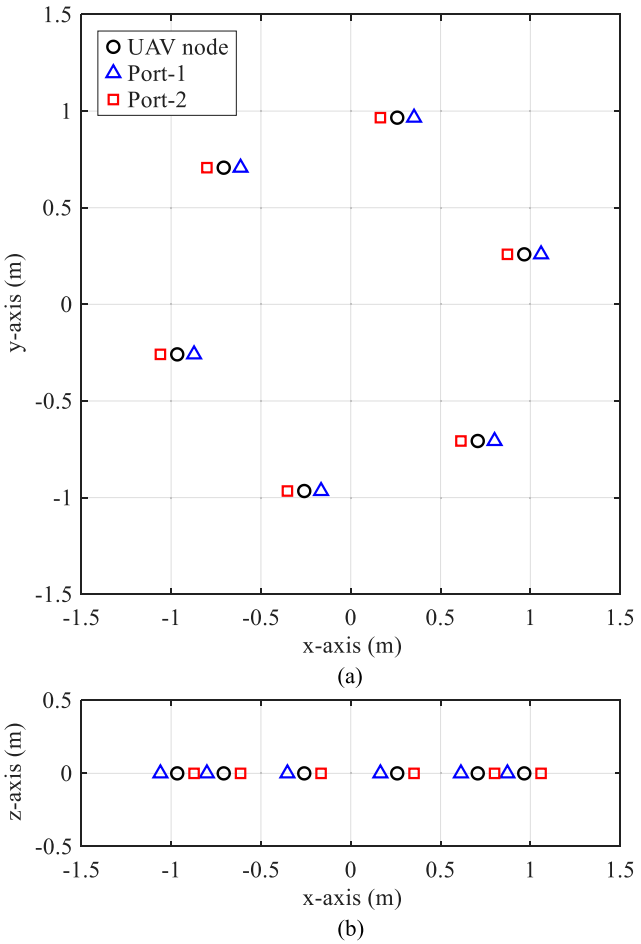


FIGURE 7. Distributed six-UAV array geometry used for the beamforming study: (a) top view of the six-node UCA and (b) front view along the boresight direction.

is fixed across all carrier frequencies. Consequently, the intra-UAV pair remains electrically compact at 0.8 GHz and 2.4 GHz, whereas the inter-UAV separation becomes electrically sparse at higher frequencies. This electrical sparsity is a primary cause of grating-lobe-like competing lobes in distributed UAV swarms, and it makes sidelobe control highly sensitive to the embedded element manifold.

A critical aspect of this study is the explicit inclusion of the complex embedded element pattern in the array manifold. The complex far-field pattern of an embedded element is written as

$$E(\theta, \phi) = |E(\theta, \phi)| e^{j\psi(\theta,\phi)}. \tag{6}$$

Here, $|E(\theta, \phi)|$ and $\psi(\theta, \phi)$ denote the magnitude and angle-dependent phase of the embedded element pattern, respectively, so that both amplitude and phase distortions are retained in the array manifold.

For the proposed case, $E_{\text{viv}}(\theta, \phi)$ is extracted from the UAV-integrated hybrid full-wave simulation described later in Section V, thereby capturing platform-induced scattering and pattern distortion.

Let $\mathbf{r}_m \in \mathbb{R}^3$ denote the position of the mth element and let $\mathbf{u}(\theta, \phi)$ denote the unit propagation vector. The manifold response of the mth element is modeled as

$$a_m(\theta, \phi) = E_m(\theta, \phi) e^{-jk\,\mathbf{u}(\theta,\phi)\cdot\mathbf{r}_m}, \tag{7}$$

where $k = 2\pi/\lambda$ is the wavenumber and $E_m(\theta, \phi)$ is the embedded element pattern. In the simulations, $E_m(\theta, \phi)$ is the complex embedded pattern of port m exported directly from the UAV-integrated full-wave model of Section V, expressed in realized gain and retaining the angle-dependent phase. No normalization is applied to it, so both the directivity of the embedded element and its angular selectivity are carried into the manifold. The isotropic baseline uses $E_m(\theta, \phi) = 1$ for all m, that is, a unit-gain element with no angular variation, which is the idealization adopted in the distributed UAV beamforming studies cited in Section I. Since the weight-design procedure, the array geometry, and the scenario parameters are identical in the two cases, the SINR and SCNR differences reported in Section VI isolate the effect of the embedded element response relative to that idealization.

The steering vector is

$$\mathbf{a}(\theta, \phi) = [a_1(\theta, \phi), \ldots, a_M(\theta, \phi)]^T. \tag{8}$$

If all elements share an identical embedded pattern $E(\theta, \phi)$, then (8) admits the factorization

$$\mathbf{a}(\theta, \phi) = E(\theta, \phi)\, \mathbf{v}(\theta, \phi), \tag{9}$$

$$\mathbf{v}(\theta, \phi) = \left[e^{-jk\mathbf{u}(\theta,\phi)\cdot\mathbf{r}_1}, \ldots, e^{-jk\mathbf{u}(\theta,\phi)\cdot\mathbf{r}_M}\right]^T, \tag{10}$$

which highlights that the embedded element response acts as a spatial pre-filter before any digital beam synthesis.

Given a complex weight vector $\mathbf{w} \in \mathbb{C}^M$, the beampattern response is

$$B(\theta, \phi) = \mathbf{w}^H \mathbf{a}(\theta, \phi) = E(\theta, \phi) \cdot \underbrace{\mathbf{w}^H \mathbf{v}(\theta, \phi)}_{AF(\theta,\phi)}. \tag{11}$$

Equation (11) clarifies the central mechanism studied in this paper: the Vivaldi embedded manifold attenuates wide-angle energy at the element level, which reduces the burden on digital weights to suppress competing lobes that arise in electrically sparse distributed swarms.

We note that the exact factorization in (9)–(11) holds only when all elements share an identical pattern. In the proposed system, Port-1 and Port-2 of each UAV exhibit slightly different embedded patterns due to the antipodal Vivaldi geometry. Accordingly, all numerical evaluations (beampattern synthesis, SINR, SCNR, and jitter analysis) use the general port-specific manifold of (7), which assigns a distinct $E_m(\theta, \phi)$ to each element. The factorized form is presented here solely to provide physical intuition for the element-level spatial filtering mechanism; it does not affect any quantitative result.

B. BEAMPATTERN SHAPE METRICS: HPBW, PSLL, AND ISL

Because the distributed UAV swarm considered in this study is planar (all elements at the same altitude) and the targets and interferers of interest lie on the horizontal plane, all beampattern metrics are evaluated on the azimuth cut at the scan elevation $\theta = \theta_0$. Accordingly, the sidelobe region is defined as the one-dimensional set $\Omega_{\mathrm{SL}} = \{\phi : |\phi - \phi_0| > \Delta\phi_{\mathrm{guard}}\}$, where $\Delta\phi_{\mathrm{guard}} = 8^\circ$ is a guard interval that excludes the mainlobe neighborhood. All integrals over Ω_{SL} in subsequent definitions reduce to line integrals over this azimuth set. This one-dimensional evaluation is consistent with the UCA geometry, in which the array has negligible aperture in the elevation dimension and therefore provides no meaningful sidelobe control in that plane.

The half-power beamwidth (HPBW) is measured as the angular width between the -3 dB points relative to the mainlobe peak on this azimuth cut.

The peak sidelobe level (PSLL) is computed as

$$\mathrm{PSLL} = 10\log_{10}\left(\frac{\max_{\phi\in\Omega_{\mathrm{SL}}} |B(\theta_0,\phi)|^2}{|B(\theta_0,\phi_0)|^2}\right). \tag{12}$$

PSLL captures the strongest competing lobe relative to the mainlobe. In distributed sensing, PSLL values close to 0 dB indicate a competing lobe comparable to the mainlobe, which can lead to ambiguity in bearing and increased susceptibility to off-boresight interference.

To quantify total sidelobe energy, we also compute the integrated sidelobe leakage (ISL),

$$\mathrm{ISL} = 10\log_{10}\left(\frac{\int_{\Omega_{\mathrm{SL}}} |B(\theta_0,\phi)|^2\, d\phi}{|B(\theta_0,\phi_0)|^2}\right), \tag{13}$$

which is more directly linked to diffuse clutter pickup because it penalizes aggregate sidelobe leakage over Ω_{SL} rather than only the peak. The ISL is used as an objective in the multi-objective weight design (Section III-E) rather than as a reported table metric, since it is implicitly captured by the SCNR result.

C. OPERATIONAL PERFORMANCE METRICS: SINR AND SCNR

The metrics in Section III-B characterize beampattern shape, but ISR/EW sensing performance is ultimately governed by how much desired signal energy is retained relative to interference, receiver noise, and, during hovering, diffuse scattering. For this reason, we evaluate two output ratios. The output signal-to-interference-plus-noise ratio (SINR) represents a point-interferer-limited regime, whereas the output signal-to-clutter-plus-noise ratio (SCNR) additionally penalizes diffuse clutter coupled through sidelobes.

Two uncorrelated narrowband interferers are placed on the same elevation cut at azimuths $\phi_{\mathrm{I},1} = -30^\circ$ and $\phi_{\mathrm{I},2} = 20^\circ$, with steering vectors $\mathbf{a}_{\mathrm{I},k} = \mathbf{a}(\theta_0, \phi_{\mathrm{I},k})$ for $k = 1, 2$. The received desired-signal power follows $P_{\mathrm{s}}(R) \propto R^{-2}$, while interferer powers $P_{\mathrm{I},k}$ and the per-element noise power σ_n^2 are held fixed across beamformers. The complete parameter values are specified in Section VI.

For a given weight vector $\mathbf{w}$, the output SINR toward the desired look direction $\mathbf{a}_0 \triangleq \mathbf{a}(\theta_0, \phi_0)$ is defined as

$$\mathrm{SINR}(\mathbf{w}; R) = \frac{P_{\mathrm{s}}(R)\,|\mathbf{w}^H\mathbf{a}_0|^2}{\sum_{k=1}^{K} P_{\mathrm{I},k}\,|\mathbf{w}^H\mathbf{a}_{\mathrm{I},k}|^2 + \sigma_n^2\|\mathbf{w}\|_2^2}. \tag{14}$$

Diffuse clutter during hovering is modeled as uniformly distributed over the azimuth sidelobe region Ω_{SL}. The corresponding output clutter power is modeled as

$$P_{\mathrm{C}}(\mathbf{w}) = \frac{\mathrm{CNR}\,\sigma_n^2}{|\Omega_{\mathrm{SL}}|}\int_{\Omega_{\mathrm{SL}}} |\mathbf{w}^H\mathbf{a}(\theta_0,\phi)|^2\, d\phi, \tag{15}$$

where CNR specifies the clutter-to-noise ratio in linear scale. With this clutter model, the output SCNR is defined as

$$\mathrm{SCNR}(\mathbf{w}; R) = \frac{P_{\mathrm{s}}(R)\,|\mathbf{w}^H\mathbf{a}_0|^2}{\sum_{k=1}^{K} P_{\mathrm{I},k}\,|\mathbf{w}^H\mathbf{a}_{\mathrm{I},k}|^2 + P_{\mathrm{C}}(\mathbf{w}) + \sigma_n^2\|\mathbf{w}\|_2^2}. \tag{16}$$

Equations (15) and (16) ensure that sidelobe leakage directly degrades sensing margin in the hovering regime, so that improvements in ISL translate into improvements in clutter-limited performance.

D. HOVERING-INDUCED POSITION UNCERTAINTY AND MONTE-CARLO PROTOCOL

To model hovering-induced formation uncertainty, each element position is perturbed by an independent zero-mean Gaussian random displacement $\Delta\mathbf{r}_m \sim \mathcal{N}(\mathbf{0}, \sigma_{\mathrm{pos}}^2\mathbf{I}_3)$ in each Monte-Carlo trial [37], [38]. Because both elements on the same UAV share a common airframe, the same perturbation vector is applied to the two co-located elements per UAV. The position-jitter standard deviation is swept from $\sigma_{\mathrm{pos}} = 0$ to 6 cm, covering the range from ideal GPS-RTK hovering ($\sigma_{\mathrm{pos}} \approx$ 1–2 cm) to degraded conditions representative of gusty or GPS-denied environments. Beamforming weights are designed on the nominal formation and then evaluated on perturbed geometries to quantify robustness against hovering-induced phase mismatch. Unless otherwise noted, the jitter-sweep plots report the mean trend over $N_{\mathrm{MC}} = 1000$ Monte-Carlo trials per σ_{pos}.

Throughout this study the swarm is assumed to be phase- and frequency-coherent, so that the position jitter above is the only source of geometric uncertainty. This assumption also makes the sweep readable as a sensitivity to residual carrier-phase error, because a residual phase offset $\Delta\varphi$ at one element is indistinguishable from a radial displacement of $\Delta\varphi\,\lambda/2\pi$: a jitter of $\sigma_{\mathrm{pos}} = 1$ cm corresponds to about 9.6° at 0.8 GHz and about 28.8° at 2.4 GHz. Airframe attitude variation enters differently. Yaw, pitch, and roll rotate the embedded element pattern with respect to the look direction rather than displacing the element, so their first-order effect is a change in the element response toward the target and toward the interferers rather than a loss of coherence across the formation. Quantifying that effect requires the embedded

pattern to be resampled over a range of airframe orientations, which is left for the field-measurement campaign described in the Conclusion.

E. BEAMFORMING WEIGHT DESIGN

1) WEIGHT PARAMETERIZATION AND NORMALIZATION

To benchmark distributed beam synthesis under sidelobe and interference constraints, four weighting strategies are evaluated: a quiescent MVDR baseline and three population-based multi-objective optimizers. The complex weight is parameterized as

$$\tilde{w}_m(\boldsymbol{\xi}) = \rho_m e^{j\varphi_m}, \quad 0 \le \rho_m \le \rho_{\max}, \quad -\pi \le \varphi_m < \pi, \tag{17}$$

where $\boldsymbol{\xi} \in \mathbb{R}^{2M}$ collects amplitudes and phases. The final weight vector is unit-norm normalized as

$$\mathbf{w}(\boldsymbol{\xi}) = \frac{\tilde{\mathbf{w}}(\boldsymbol{\xi})}{\|\tilde{\mathbf{w}}(\boldsymbol{\xi})\|_2}, \tag{18}$$

so that interference, clutter, and noise terms in (14) and (16) are compared under a common weight-norm constraint.

2) QUIESCENT MVDR BASELINE

The MVDR beamformer minimizes output power under a distortionless constraint in the look direction:

$$\mathbf{w}_{\mathrm{MVDR}} = \frac{\mathbf{R}^{-1}\mathbf{a}(\theta_0, \phi_0)}{\mathbf{a}^H(\theta_0, \phi_0)\mathbf{R}^{-1}\mathbf{a}(\theta_0, \phi_0)}. \tag{19}$$

In this work, $\mathbf{R}$ is implemented as a data-independent quiescent covariance model with diagonal loading [39], providing a stable closed-form reference that isolates the impact of the embedded manifold on the synthesized beampattern.

3) MULTI-OBJECTIVE FORMULATION WITH OPERATIONAL AWARENESS

Sparse distributed swarms face an inherent trade-off between maintaining look-direction response and suppressing sidelobe leakage that drives interference and clutter pickup. Accordingly, the weight design is posed as a multi-objective optimization:

$$\min_{\boldsymbol{\xi}} \mathbf{f}(\boldsymbol{\xi}) = \left[f_{\mathrm{PSLL}}(\boldsymbol{\xi}),\ f_{\mathrm{ISL}}(\boldsymbol{\xi}),\ f_{\mathrm{OP}}(\boldsymbol{\xi})\right]^T, \tag{20}$$

where $f_{\mathrm{PSLL}}(\boldsymbol{\xi}) = \mathrm{PSLL}(\mathbf{w}(\boldsymbol{\xi}))$ and $f_{\mathrm{ISL}}(\boldsymbol{\xi}) = \mathrm{ISL}(\mathbf{w}(\boldsymbol{\xi}))$ follow (12) and (13). The operational objective is set as

$$f_{\mathrm{OP}}(\boldsymbol{\xi}) = -\mathrm{SINR}(\mathbf{w}(\boldsymbol{\xi})) \tag{21}$$

for the point-interferer regime, while it is replaced by $-\mathrm{SCNR}(\mathbf{w}(\boldsymbol{\xi}))$ when clutter-limited hovering is emphasized.

4) OPTIMIZATION ALGORITHMS

Three population-based metaheuristics are employed:

- **NSGA-III:** A non-dominated sorting genetic algorithm (NSGA) that maintains diversity over the Pareto set and provides stable convergence in many-objective trade spaces [40].
- **MOPSO:** A multi-objective particle swarm optimizer (MOPSO) that evolves candidate weights using velocity-position updates guided by an external archive of non-dominated leaders [41].
- **MOEA/D:** A decomposition-based multi-objective evolutionary algorithm (MOEA) that solves a set of scalarized subproblems cooperatively through neighborhood updates [42].

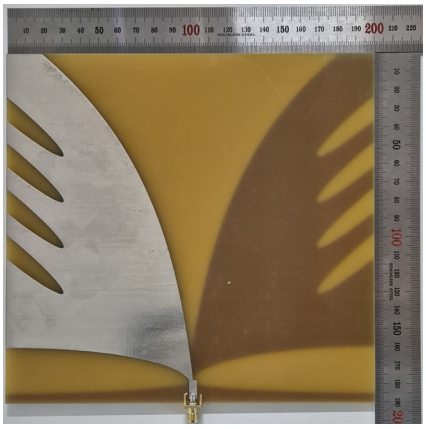
The purpose of including multiple optimizers is not to advocate a universally superior solver, but to verify that the manifold-level benefit of the proposed UAV-integrated Vivaldi antenna persists across different weight-synthesis mechanisms.

All three optimizers share a population size of 200 individuals and run for 500 generations (or iterations for MOPSO). For NSGA-III, reference points are generated by Das and Dennis's systematic approach with four divisions per objective, yielding 15 reference directions on the three-objective simplex; the simulated binary crossover probability is $p_c = 0.9$ (distribution index $\eta_c = 20$) and the polynomial mutation probability is $p_m = 1/(2M)$ (distribution index $\eta_m = 20$). For MOPSO, the inertia weight is $w = 0.4$, the cognitive and social coefficients are $c_1 = c_2 = 1.5$, and the external archive capacity is 200. For MOEA/D, the Tchebycheff scalarization is adopted with a neighborhood size of 20; the weight vectors are uniformly distributed on the three-objective simplex using the same Das–Dennis scheme as NSGA-III. Each optimizer is executed with five independent random seeds, and the run yielding the best hypervolume indicator is retained. The values reported for the three stochastic optimizers therefore correspond to the best-hypervolume run and represent an upper bound on the performance attainable by each solver, whereas the MVDR baseline is deterministic and carries no such run-to-run variation.

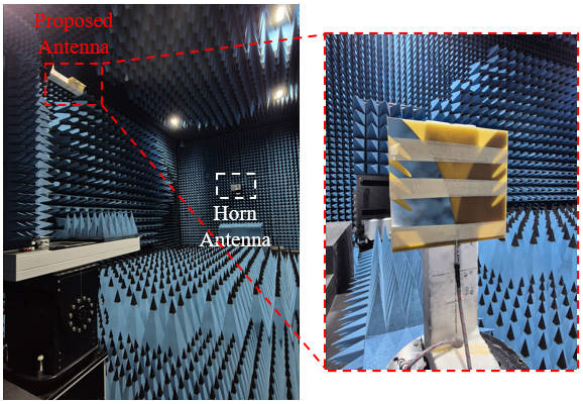
Because the optimization produces a three-dimensional Pareto front (PSLL, ISL, f_{OP}), a single operating-point solution must be selected for the beampattern and table comparisons. We adopt the normalized-distance knee-point selection: each Pareto-optimal objective vector is normalized to $[0, 1]$ by the utopia and nadir points of the front, and the solution with the minimum Euclidean distance to the utopia point is chosen as the representative knee solution. This procedure yields a balanced trade-off among the three objectives without requiring manual preference articulation. The ISL values at the selected knee points range from -6.1 to -9.8 dB across all configurations; because these values are strongly correlated with the reported SCNR (lower ISL corresponds to higher SCNR), ISL is omitted from Table 4 to avoid redundancy.

IV. FABRICATION AND MEASUREMENT

Having established the beamforming framework in the preceding section, we now validate the antenna design through fabrication and measurement. The prototype is fabricated on a single 2.4 mm-thick FR-4 laminate with the



(a)



(b)

FIGURE 8. (a) Photograph of the fabricated wing-shaped antipodal Vivaldi antenna. (b) Measurement setup in the anechoic chamber.

dimensions of Table 1, fed by an SMA connector at the microstrip feed line, and all simulations reported in this work are obtained with CST Microwave Studio using the same dimensions. Fig. 8(a) shows the fabricated prototype of the proposed antenna, while Fig. 8(b) illustrates the measurement setup in an anechoic chamber.

Fig. 9 compares the measured and simulated reflection coefficient and maximum realized gain of the proposed antenna. The measured results confirm that the antenna operates over a wide frequency range from 0.4 GHz to 7.3 GHz, showing good agreement with the simulated results. In addition, the measured maximum realized gain follows a similar trend to the simulated response across the operating band, validating the wideband and stable radiation performance of the proposed design.

Fig. 10(a)–(d) show the measured radiation patterns at 0.8 GHz, 1.2 GHz, 2.4 GHz, and 5.8 GHz, respectively. As can be seen, stable end-fire radiation characteristics are achieved over all measured frequencies. The measured patterns closely match the simulated results, demonstrating the effectiveness of the proposed design in realizing wideband end-fire radiation behavior.

Several recent studies have reported wideband Vivaldi antennas using various geometry optimization and loading

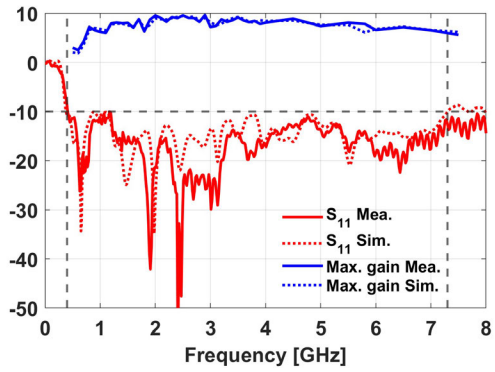


FIGURE 9. Comparison of reflection coefficient and maximum realized gain between measurement and simulation.

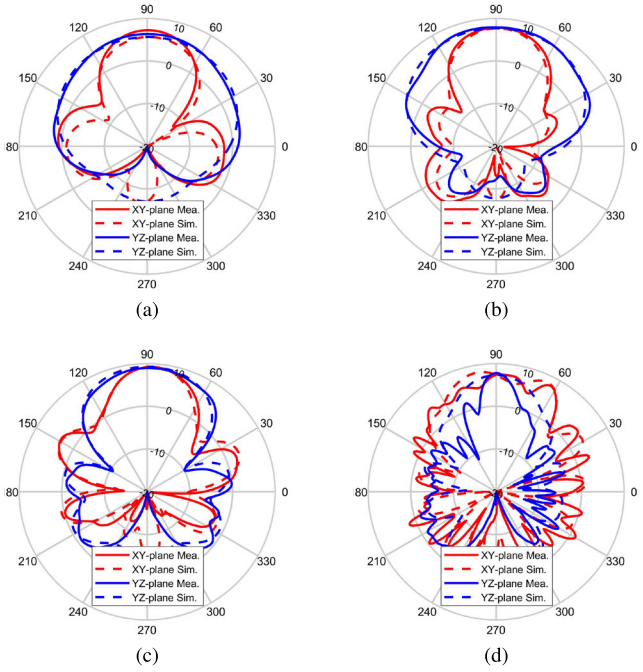


FIGURE 10. Measured radiation patterns of the proposed antenna at (a) 0.8 GHz, (b) 1.2 GHz, (c) 2.4 GHz, and (d) 5.8 GHz.

techniques, as summarized in Table 2. The bandwidth-to-volume ratio (BVR), defined as the ratio of fractional bandwidth (FBW, %) to the electrical volume (λ_0^3) and scaled by 10^{-4} for clarity, is used to provide a fair comparison of bandwidth efficiency.

In [21], a compact antenna is achieved through nonuniform slot-profile optimization; however, the small aperture size results in relatively low realized gain. In [23], a high-permittivity substrate ($\varepsilon_r = 10.2$) is employed to shift the operating band toward lower frequencies, although limited discussion is provided on radiation characteristics, making it difficult to verify stable end-fire behavior under free-space conditions.

The proposed antenna provides the widest fractional bandwidth among the compared works, and most reported designs [22], [24], [25], [26], [27] exhibit lower BVRs

TABLE 2. Comparison of the proposed antenna with previously reported Vivaldi antennas.

No.	Year	Size (mm^3)	Permittivity (ε_r)	Max. Gain (dBi)	Frequency (GHz)	FBW (%)	Electrical Volume (λ_0^3)	BVR ($\times 10^{-4}$)	Platform
[27]	2021	$55 \times 30 \times 0.508$	3.38	12.7	4.5–50	166.97	$0.825 \times 0.45 \times 0.008$	5.9	×
[25]	2023	$300 \times 237.6 \times 1.5$	2.2	12.3	0.9–4	126.53	$0.9 \times 0.713 \times 0.005$	4.38	×
[24]	2024	$615.6 \times 650 \times 1.6$	4.4	7.59	0.3–0.7	80	$0.616 \times 0.65 \times 0.002$	12.5	×
[23]	2024	$60 \times 40 \times 1.905$	10.2	N/A	0.53–5	161.66	$0.106 \times 0.07 \times 0.003$	641.3	○
[22]	2025	$180 \times 82 \times 1$	3.55	14.3	2–20	163.64	$1.2 \times 0.547 \times 0.007$	3.74	×
[26]	2025	$38 \times 25 \times 4.0$	4.4	9.6	2.81–13.6	131.51	$0.356 \times 0.234 \times 0.0375$	4.21	×
[21]	2025	$17 \times 29.5 \times 0.813$	3.55	6.8	3.12–25.6	156.55	$0.177 \times 0.307 \times 0.0085$	34.06	×
[9]	2026	$68 \times 52 \times 0.25$	3.5	12	2–18	160.00	$0.45 \times 0.34 \times 0.0016$	65.36	○
This work	**2026**	$190 \times 200 \times 2.4$	4.4	9.6	0.4–7.3	179.22	$0.253 \times 0.267 \times 0.0032$	82.90	○

than the proposed antenna, indicating limited bandwidth efficiency when the electrical size is taken into account. These approaches primarily rely on slot loading, taper optimization, dielectric loading, or artificial electromagnetic materials to enhance bandwidth or gain. While such methods can improve impedance or radiation performance, they often increase structural complexity and do not explicitly address the underlying radiation mechanism governing broadband end-fire operation.

Furthermore, in many existing designs, radiation characteristics are optimized through empirical parameter tuning rather than physics-based modal control. As a result, the mechanism responsible for stable end-fire radiation across the operating band remains unclear, particularly at low frequencies. In addition, most prior works are evaluated under free-space conditions, leaving their performance under practical platform environments largely unexplored.

Table 3 summarizes the design methodology and validation scope of the same works, which the quantitative metrics in Table 2 do not capture. It shows that the compared works pursue different design objectives through geometry-driven modifications and are validated at the element level, whereas the present work identifies and controls the dominant radiation mode and extends the evaluation to a platform-integrated element and a distributed array manifold.

In contrast, the proposed antenna adopts a CMA-driven design approach to explicitly control the dominant radiation modes, enabling stable end-fire radiation at low frequencies while maintaining ultra-wideband impedance characteristics. These two requirements are in conflict in tapered-slot antennas. Lowering the cutoff frequency requires a larger or more gradually tapered aperture, but at the newly added low-frequency edge the aperture becomes electrically small and the dominant mode reverts to a broadside distribution, so the end-fire directivity degrades precisely where the band has been extended. Instead of enlarging the aperture or adding dielectric loading, which increases size, weight, and loss, the proposed design redirects the surface current of the offending mode along the longitudinal axis so that the same mode contributes to end-fire radiation. This is why the widest fractional bandwidth in Table 2 is obtained together with stable end-fire radiation at an electrical size of $0.25\lambda_0$ on a single-layer substrate.

Moreover, beyond conventional free-space validation, the proposed design is further evaluated in a UAV-integrated environment, demonstrating its robustness against platform-induced scattering and its effectiveness in distributed beamforming scenarios in the following sections.

The advantages of the proposed design and the accompanying design trade-offs, with respect to the works listed in Tables 2 and 3, are summarized as follows.

Advantages:

- The widest fractional bandwidth among the compared works is obtained at an electrical size of $0.25\lambda_0$ on a single-layer substrate, without dielectric loading or multilayer stacking.
- The low-frequency radiation instability is resolved at its modal origin rather than by parametric tuning, so the mechanism behind the stable end-fire behavior is identified rather than inferred.
- The embedded element pattern is extracted with the antenna mounted on a UAV, whereas only [9] among the compared works characterizes the element on a host platform.
- Element-level directivity is carried through to system-level sensing metrics in a distributed swarm, which none of the compared works reports.

Limitations:

- Because the operating band is extended down to 0.4 GHz, the physical footprint is larger than that of the compared designs whose lower edge lies above 1.8 GHz, even though the electrical size remains among the smallest in Table 2.
- Because the aperture is kept electrically compact to preserve bandwidth efficiency, the maximum realized gain is lower than that of the compared designs built on substantially larger electrical apertures [22], [27].

V. UAV PLATFORM INTEGRATION

The measured results confirm that the proposed antenna provides stable impedance and end-fire radiation characteristics over the ultra-wide operating band. Based on these results, the antenna is expected to be suitable for wideband directional communication and sensing applications. Therefore, to further investigate its applicability in practical scenarios, the proposed antenna is integrated into a representative

TABLE 3. Comparison of the design approach, design objective, and validation scope with previously reported Vivaldi antennas.

No.	Design approach	Primary design objective	Validation scope
[27]	Scattering-structure design	Signature reduction	Free-space element and array
[25]	Material and structural loading	Gain enhancement	Free-space element and array
[24]	Aperture profile shaping	Size reduction	Free-space element
[23]	Material and structural loading	Size reduction	Element in coupling medium
[22]	Aperture profile shaping	Bandwidth extension	Free-space element
[26]	Material and structural loading	Gain enhancement	Free-space element
[21]	Aperture profile shaping	Size reduction	Free-space element
[9]	Material and structural loading	Signature reduction	UAV-integrated element
This work	**Modal control**	**Bandwidth with end-fire stability**	**UAV-integrated element and array**

UAV platform (Tarot X4) and analyzed through full-wave electromagnetic simulations. The antenna is mounted along the longitudinal axis of the UAV to preserve the end-fire radiation direction and to emulate a forward-looking EW configuration.

Fig. 11 shows the Tarot X4 UAV platform integrated with the proposed antenna configuration. The antenna elements are arranged with an inter-element spacing G_A corresponding to a half-wavelength at 5.8 GHz, which is the highest frequency among the operating bands of interest (0.8 GHz, 1.2 GHz, 2.4 GHz, and 5.8 GHz). Accordingly, the spacing is set to $G_A = 25.86$ mm. This spacing suppresses grating lobes within the beam-scanning range while maintaining compact array spacing across the operating band. Based on this configuration, beamforming performance is evaluated at 0.8 GHz and 2.4 GHz as representative frequencies within the operating band.

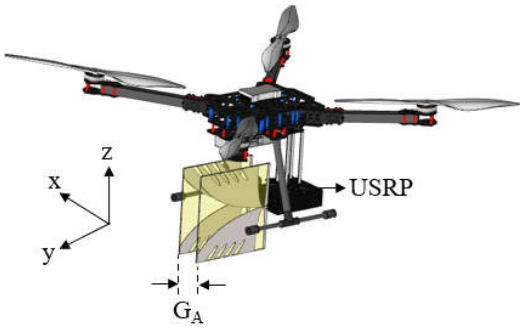


FIGURE 11. Tarot X4 UAV platform integrated with the proposed antenna configuration. The element spacing G_A corresponds to half-wavelength at 5.8 GHz (25.86 mm).

To evaluate the mutual coupling and beamforming performance under excitation conditions, the active reflection coefficient is employed, which is defined as

$$S_{\text{active},i} = \sum_{j=1}^{N} S_{ij} e^{j(\phi_j - \phi_i)}, \tag{22}$$

where S_{ij} denotes the scattering parameter between the i-th and j-th ports, ϕ_i and ϕ_j represent the excitation phases, and N is the total number of antenna elements [43], [44].

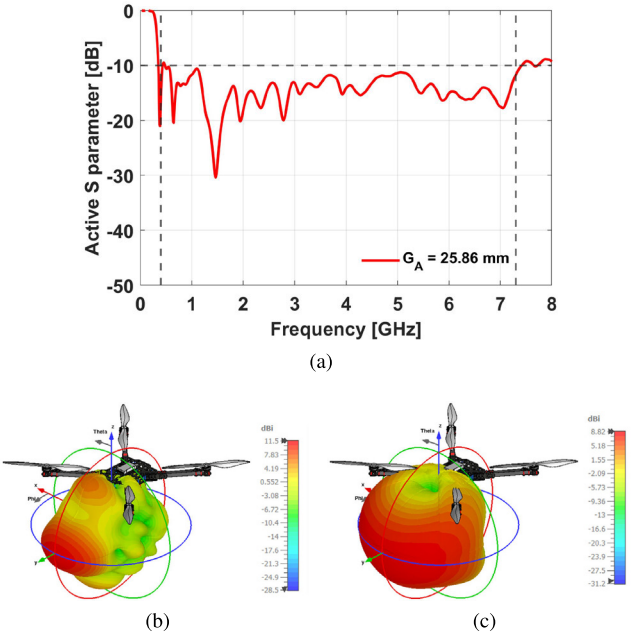


FIGURE 12. Simulated performance of the proposed antenna integrated with the UAV platform: (a) active S-parameter, (b) radiation pattern at 0.8 GHz, and (c) radiation pattern at 2.4 GHz.

Fig. 12(a) presents the simulated active S-parameters of the proposed antenna mounted on the UAV platform. It is observed that the active reflection coefficient remains below -10 dB over the operating band, confirming stable impedance characteristics under beamforming excitation while inherently accounting for mutual coupling among antenna elements.

Fig. 12(b) and (c) illustrate the simulated radiation patterns at 0.8 GHz and 2.4 GHz, respectively. It is observed that a directional beam is successfully formed at both frequencies while maintaining the desired end-fire radiation behavior, demonstrating the feasibility of the proposed antenna for UAV-based EW applications. Based on the UAV-mounted antenna configuration evaluated above, the beamforming capability of the proposed antenna array is further investigated in the following section.

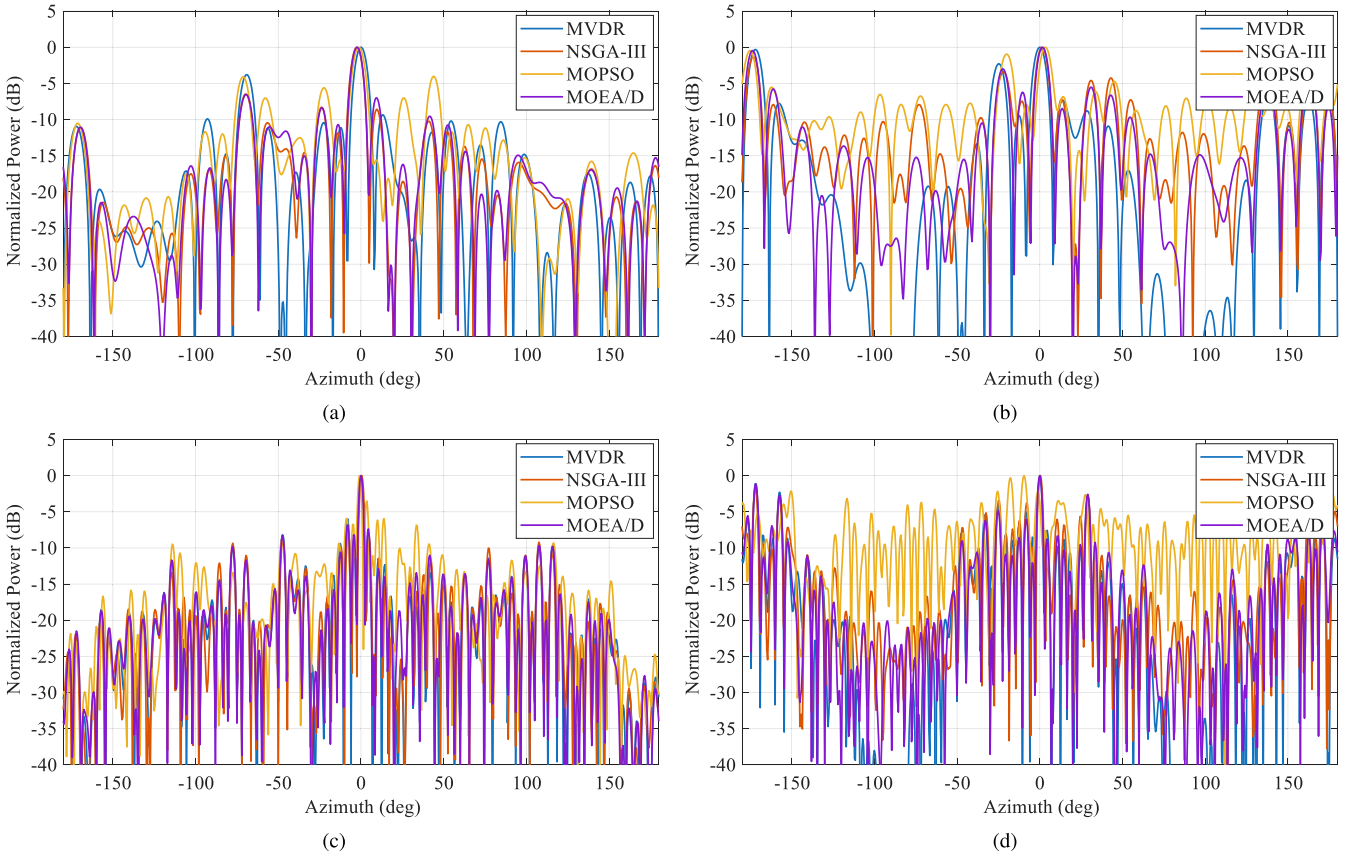


FIGURE 13. Normalized synthesized azimuth-cut beampatterns for the UCA deployment under MVDR and three multi-objective optimizers, comparing the proposed UAV-integrated Vivaldi embedded manifold with an isotropic baseline. (a) Vivaldi, 0.8 GHz. (b) Isotropic, 0.8 GHz. (c) Vivaldi, 2.4 GHz. (d) Isotropic, 2.4 GHz.

VI. EW SIMULATION RESULTS

A. BEAM SYNTHESIS PERFORMANCE COMPARISON

Fig. 13 compares the nominal synthesized azimuth-cut beampatterns for the UCA formation at 0.8 GHz and 2.4 GHz. These plots enable direct visual assessment of three properties that are operationally relevant in ISR/EW sensing: mainlobe sharpness, the presence of competing lobes, and wide-angle leakage.

First, the difference between the Vivaldi and isotropic manifolds is most apparent when comparing panels (a) and (b), and panels (c) and (d). The Vivaldi case consistently exhibits lower wide-angle response because the embedded pattern factor in (11) suppresses energy before the digital weights act. In contrast, the isotropic case relies solely on digital cancellation, which becomes fragile when the distributed aperture is electrically sparse.

Second, the impact of electrical sparsity is revealed by comparing the 0.8 GHz panels to the 2.4 GHz panels. At 2.4 GHz, the inter-UAV spacing corresponds to many wavelengths, so the isotropic baseline produces pronounced competing lobes and a dense sidelobe structure. This effect is particularly clear in Fig. 13(d), which is consistent with Table 4: the isotropic UCA at 2.4 GHz yields PSLL values near 0 dB for MOPSO, indicating a sidelobe comparable to the mainlobe and significant ambiguity risk. In the same configuration, the Vivaldi manifold in Fig. 13(c) maintains PSLL between -5.92 dB and -8.97 dB, which indicates a substantially lower risk of bearing ambiguity and a lower probability of clutter pickup through competing lobes.

Third, the effect of operating frequency is reflected in mainlobe width: the UCA HPBW contracts from approximately 6.9°–7.6° at 0.8 GHz to 2.4°–3.5° at 2.4 GHz, as seen in Table 4. A narrower mainlobe improves angular selectivity for target bearing estimation, while the risk of clutter pickup through sidelobes increases unless sidelobes are well controlled.

B. RANGE-DEPENDENT SINR AND SCNR PERFORMANCE

Fig. 14 reports the output SINR while sweeping the target range R. Since $P_s(R) \propto R^{-2}$ and the interference-plus-noise terms are held fixed, all curves decay monotonically with range [45].

At 0.8 GHz, the Vivaldi manifold provides a consistent SINR uplift: MVDR improves from 6.51 dB (isotropic) to 16.31 dB (Vivaldi)—a gain of 9.80 dB obtained without any change to the weight-design procedure and therefore attributable to the embedded element response alone. The Vivaldi NSGA-III and MOEA/D solutions reach 27.09 dB and 26.64 dB, respectively, and remain above 10 dB throughout the full sweep to 500 m. At 2.4 GHz, electrical

TABLE 4. Beamforming performance summary for the six-UAV UCA swarm ($M = 12$ elements) at 0.8 and 2.4 GHz.

f (GHz)	Antenna	Method	HPBW (deg)	PSLL (dB)	SINR (dB)	SCNR (dB)	Jitter Loss (dB)
0.8	Vivaldi	MVDR	7.48	-3.79	16.31	14.28	0.15
		NSGA-III	7.09	-6.47	27.09	17.23	0.15
		MOPSO	7.52	-4.03	18.57	13.46	0.14
		MOEA/D	6.86	-6.53	26.64	16.88	0.15
	Isotropic	MVDR	7.64	-0.31	6.51	5.95	0.15
		NSGA-III	7.03	-1.32	20.70	12.00	0.13
		MOPSO	7.35	-0.47	16.75	8.20	0.09
		MOEA/D	6.95	-0.46	21.22	12.67	0.12
2.4	Vivaldi	MVDR	2.56	-6.20	20.14	10.05	1.40
		NSGA-III	2.61	-8.97	22.87	9.93	1.39
		MOPSO	2.40	-5.92	13.69	6.01	0.85
		MOEA/D	2.52	-7.14	21.31	10.02	1.39
	Isotropic	MVDR	2.57	-1.12	10.05	3.97	1.37
		NSGA-III	2.72	-1.80	11.68	3.71	1.20
		MOPSO	3.45	0.00	6.58	-3.51	0.58
		MOEA/D	2.68	-1.19	12.21	4.20	1.36

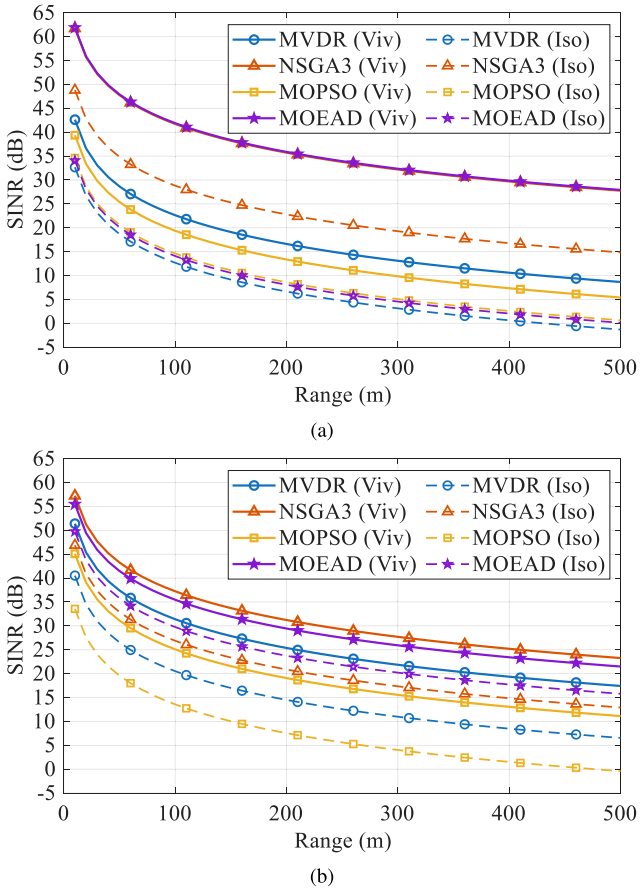


FIGURE 14. Output SINR versus target range for the UCA swarm configuration under two interferers at −30° and 20° azimuth. Solid curves denote the Vivaldi embedded manifold, and dashed curves denote the isotropic baseline. (a) SINR at 0.8 GHz; (b) SINR at 2.4 GHz.

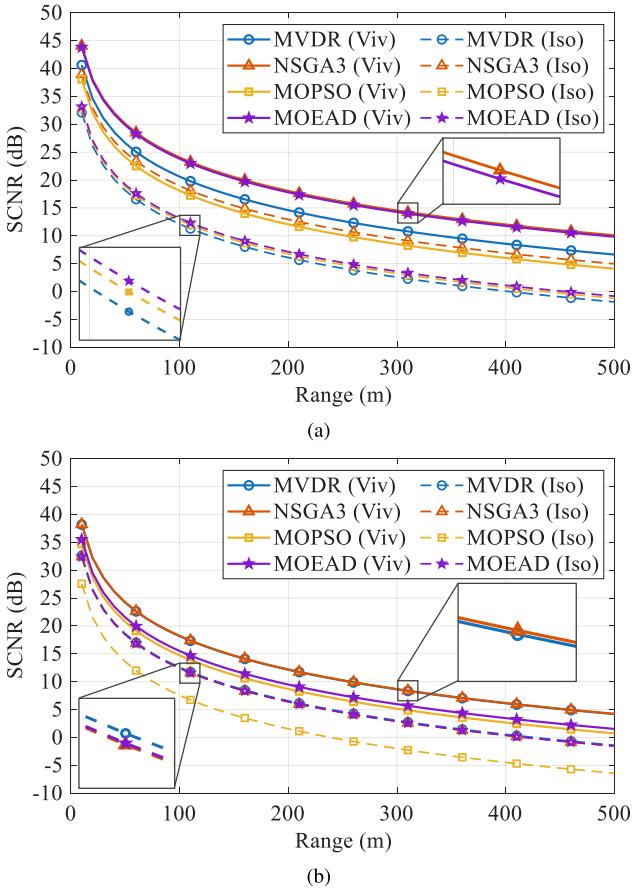


FIGURE 15. Output SCNR versus target range for the UCA swarm configuration under diffuse clutter and two interferers at −30° and 20° azimuth. Solid curves denote the Vivaldi embedded manifold, and dashed curves denote the isotropic baseline. (a) SCNR at 0.8 GHz; (b) SCNR at 2.4 GHz.

sparsity makes the isotropic baseline increasingly vulnerable to competing lobes: isotropic MVDR is limited to 10.05 dB and MOPSO to 6.58 dB, whereas Vivaldi NSGA-III and MOEA/D achieve 22.87 dB and 21.31 dB.

Fig. 15 evaluates the same sensing task in a clutter-limited hovering environment. Unlike SINR, SCNR penalizes total sidelobe leakage through the clutter integral in (15), revealing vulnerabilities hidden by point-interferer metrics alone. At 0.8 GHz, Vivaldi MVDR achieves 14.28 dB SCNR versus 5.95 dB for isotropic MVDR. The most diagnostic case is 2.4 GHz: the isotropic manifold produces negative SCNR for MOPSO (−3.51 dB) despite positive SINR, directly demonstrating that deep nulls at interferer angles can

coexist with large aggregate sidelobe leakage. The Vivaldi manifold maintains positive SCNR for all methods, with 9.93 dB for NSGA-III and 10.02 dB for MOEA/D. Using 3 dB as a practical hovering criterion, the Vivaldi manifold supports a clutter-limited range of 440–450 m, compared with 220–230 m for the strongest isotropic solutions. These figures are specific to the scenario parameters listed in Section VI-D, in particular CNR = 20 dB, and are not a general operating range. Because the output clutter power in (15) scales linearly with CNR while the desired power scales as R^{-2}, the range at which a given SCNR threshold is met varies as $\mathrm{CNR}^{-1/2}$ in the clutter-dominated regime, so a 10 dB increase in CNR shortens it by roughly a factor of three. At low CNR the clutter term falls below the interference and noise terms and the behavior approaches the SINR curves of Fig. 14. The ratio between the Vivaldi and isotropic ranges is far less sensitive to this choice, since the clutter term enters both cases in the same way.

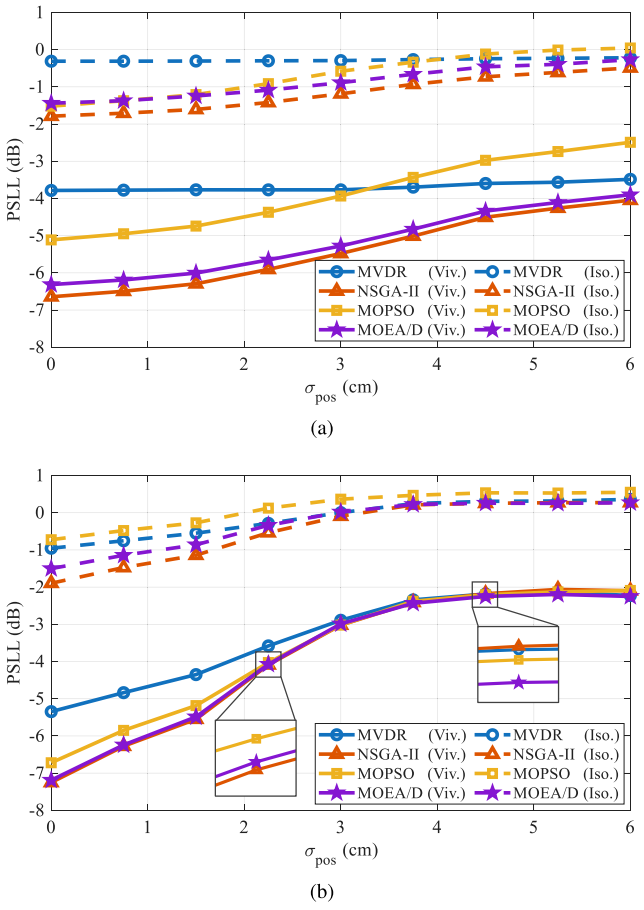


FIGURE 16. Sensitivity of PSLL to hovering-induced position uncertainty for the UCA swarm configuration. Solid curves denote the Vivaldi embedded manifold, and dashed curves denote the isotropic baseline. (a) 0.8 GHz and (b) 2.4 GHz.

C. ROBUSTNESS TO HOVERING-INDUCED POSITION JITTER

Fig. 16 quantifies how hovering-induced position errors degrade sidelobe control. PSLL degrades much more rapidly at 2.4 GHz than at 0.8 GHz because the same absolute position perturbation corresponds to a larger fraction of a wavelength, consistent with the jitter-loss values in Table 4 (below 0.15 dB at 0.8 GHz, exceeding 1 dB at 2.4 GHz).

For the isotropic UCA at 2.4 GHz, PSLL starts near 0 dB even without jitter, indicating that the nominal beampattern is already ambiguity-prone. The Vivaldi UCA starts between −5.92 dB and −8.97 dB depending on the beamformer, preserving a nontrivial sidelobe margin over the full jitter sweep. This confirms that element-level spatial selectivity can partially compensate for coherence loss by suppressing wide-angle energy before it enters the digital synthesis stage.

D. COMPARISON AT A FIXED OPERATING POINT

Table 4 summarizes the nominal beampattern metrics and the operational performance at a fixed operating point. HPBW and PSLL are evaluated from the nominal (jitter-free) beampatterns. SINR and SCNR are obtained by linear-domain averaging over $N_{\mathrm{MC}} = 1000$ Monte-Carlo trials and then converted to dB. The jitter-loss column reports the mean mainlobe gain degradation under $\sigma_{\mathrm{pos}} = 3$ cm position uncertainty.

The scenario parameters are as follows. A desired emitter at range $R_0 = 200$ m produces a received signal power of $P_{\mathrm{s}}(R_0) = -70$ dBm per element, scaled as $P_{\mathrm{s}}(R) = P_{\mathrm{s}}(R_0)(R_0/R)^2$ for the range sweep. Two uncorrelated narrowband interferers (BW = 1 MHz) at azimuths −30° and 20° each contribute $P_{\mathrm{I},k} = -50$ dBm per element, representing strong co-channel emitters 20 dB above the desired signal at the reference range. The per-element noise power is $\sigma_n^2 = -100$ dBm (consistent with a 1 MHz noise bandwidth and a receiver noise figure of approximately 4 dB at $T_0 = 290$ K). The clutter-to-noise ratio is set to CNR = 20 dB (linear: 100), representing a moderately cluttered hovering environment. All powers are defined at the element level prior to beamforming, and the unit-norm weight constraint $\|\mathbf{w}\|_2 = 1$ ensures that the reported SINR and SCNR values are directly comparable across methods.

The SINR and SCNR values are obtained by linear-domain averaging over all trials and then converting to dB via (23):

$$\gamma_{\mathrm{avg,dB}} = 10\log_{10}\left(\frac{1}{N_{\mathrm{MC}}}\sum_{n=1}^{N_{\mathrm{MC}}}\gamma_{\mathrm{lin}}^{(n)}\right). \tag{23}$$

The standard deviations of the jitter-loss values across 1000 trials are below 0.08 dB at 0.8 GHz and below 0.45 dB at 2.4 GHz for all methods, and the 95% confidence intervals of the mean are narrower than ±0.03 dB in all cases. The $\pm 1\sigma$ envelopes of the PSLL curves in Fig. 16 remain below 0.5 dB and are omitted to avoid visual clutter.

Across both bands, the Vivaldi manifold consistently outperforms the isotropic baseline. The most revealing case is 2.4 GHz, where the isotropic MOPSO yields PSLL = 0 dB and SCNR = −3.51 dB despite positive SINR—confirming that aggregate sidelobe leakage, not point-interferer suppression, is the limiting factor. The Vivaldi manifold preserves

positive SCNR for all methods, reinforcing that its primary system-level benefit is reduced wide-angle leakage.

E. OPERATIONAL INTERPRETATION FOR UAV HOVERING SENSING

The combined results support three ISR/EW-relevant conclusions. First, in a point-interferer regime, SINR can be improved by suppressing a small set of discrete angles, so a closed-form baseline can remain competitive when the formation is not severely sparse. Second, in clutter-limited hovering, SCNR is the more faithful operational metric because it penalizes total sidelobe leakage through (15). Third, the proposed Vivaldi antenna should be interpreted primarily as a manifold-shaping component for distributed sensing. Its embedded directivity and platform-aware scattering effects reduce wide-angle pickup, which translates into lower PSLL, higher SCNR, and improved viability of distributed beam synthesis in electrically sparse UAV formations.

The 0.4–7.3 GHz coverage maps onto the bands an ISR/EW payload has to monitor, from UHF emitters to the 2.4 and 5.8 GHz small-UAS links, so a single element replaces the several narrowband antennas that a UAV payload would otherwise carry. Combined with the clutter-limited range of 440–450 m reported above, this defines the standoff at which a six-node formation can perform direction finding and signal interception while hovering. The beamforming study itself is carried out at 0.8 and 2.4 GHz, which bracket the electrically compact and the electrically sparse regimes of the formation; the coverage statement above therefore refers to the impedance and radiation bandwidth of the element, which is supported by the measurements of Section IV, and not to a demonstrated beamforming result at 5.8 GHz. At that frequency the inter-UAV separation is larger still, so the competing-lobe behavior already visible at 2.4 GHz would be more pronounced and the element-level suppression correspondingly more important. The underlying procedure, identifying the dominant mode, verifying its excitation, and reorienting its surface current, applies to any tapered-slot radiator whose low-frequency pattern degrades in the same way.

VII. CONCLUSION

This paper presents a CMA-driven design approach for a compact wideband antipodal Vivaldi antenna intended for UAV-based ISR and EW applications. By leveraging characteristic mode analysis, the degraded end-fire radiation at low frequencies is identified as being dominated by a broadside radiation mode with vertically oriented surface currents. This physical insight enables targeted modification of the current distribution through a wing-shaped resonator, resulting in stable end-fire radiation without degrading higher-frequency performance.

The proposed antenna achieves ultra-wideband operation from 0.4 to 7.3 GHz (FBW: 179%) with a maximum realized gain of 9.6 dBi, while maintaining stable end-fire radiation across representative ISR/EW frequency bands. The design is experimentally validated, showing good agreement between simulated and measured results.

Furthermore, the antenna performance is evaluated by full-wave simulation in a UAV-integrated environment, indicating that platform-induced effects are effectively mitigated while preserving the desired radiation behavior. The simulation results indicate that the antenna acts as a spatial pre-filter, shaping the effective array manifold and improving directional signal collection and interference suppression in distributed UAV-based sensing systems. These findings highlight the importance of jointly considering antenna design and beamforming performance, establishing a joint antenna and beamforming design perspective as a practical consideration for future UAV-based EW/ISR applications.

Future work will include experimental validation of the UAV-mounted configuration through field measurements with a physical multi-UAV swarm prototype.

ACKNOWLEDGMENT

The authors would like to thank the Defense Acquisition Program Administration (DAPA) for motivating this research.

REFERENCES

[1] A. E. Spezio, "Electronic warfare systems," *IEEE Trans. Microw. Theory Techn.*, vol. 50, no. 3, pp. 633–644, Mar. 2002.
[2] Y. Saleem, M. H. Rehmani, and S. Zeadally, "Integration of cognitive radio technology with unmanned aerial vehicles: Issues, opportunities, and future research challenges," *J. Netw. Comput. Appl.*, vol. 50, pp. 15–31, Apr. 2015.
[3] A. Yu, I. Kolotylo, H. A. Hashim, and A. E. E. Eltoukhy, "Electronic warfare cyberattacks, countermeasures, and modern defensive strategies of UAV avionics: A survey," *IEEE Access*, vol. 13, pp. 68660–68681, 2025.
[4] A. A. Laghari, A. K. Jumani, R. A. Laghari, and H. Nawaz, "Unmanned aerial vehicles: A review," *Cognit. Robot.*, vol. 3, pp. 8–22, Jan. 2023.
[5] Z. Yang, J. Zheng, Y. Yang, T. Zhang, J. Yang, H. Liu, K. C. Ho, and Q. Gao, "Beamforming for unmanned aerial vehicle swarm-based distributed radar array: Theoretical analysis and engineering demonstration," *IEEE Trans. Aerosp. Electron. Syst.*, vol. 60, no. 6, pp. 8976–8991, Dec. 2024.
[6] S. Mohanti, C. Bocanegra, J. Meyer, G. Secinti, M. Diddi, H. Singh, and K. Chowdhury, "AirBeam: Experimental demonstration of distributed beamforming by a swarm of UAVs," in *Proc. IEEE 16th Int. Conf. Mobile Ad Hoc Sensor Syst. (MASS)*, Nov. 2019, pp. 162–170.
[7] Q. Shen, W. Liu, L. Wang, and Y. Liu, "Adaptive beamforming for target detection and surveillance based on distributed unmanned aerial vehicle platforms," *IEEE Access*, vol. 6, pp. 60812–60823, 2018.
[8] V. R. Kandregula, Z. D. Zaharis, Q. Z. Ahmed, F. A. Khan, T. H. Loh, J. Schreiber, A. J. R. Serres, and P. I. Lazaridis, "A review of unmanned aerial vehicle based antenna and propagation measurements," *Sensors*, vol. 24, no. 22, pp. 7395–7421, Nov. 2024.
[9] M. K. Rauniyar, K. K. Suman, and R. K. Gangwar, "Advanced packaging of conformal wideband antennas for UAVs with optimized RCS reduction," *IEEE Trans. Compon., Packag., Manuf. Technol.*, vol. 16, no. 1, pp. 122–130, Jan. 2026.
[10] K. Meng, Q. Wu, J. Xu, W. Chen, Z. Feng, R. Schober, and A. L. Swindlehurst, "UAV-enabled integrated sensing and communication: Opportunities and challenges," *IEEE Wireless Commun.*, vol. 31, no. 2, pp. 97–104, Apr. 2024.
[11] J. Peng, Z. Zhang, Q. Wu, and B. Zhang, "Anti-jamming communications in UAV swarms: A reinforcement learning approach," *IEEE Access*, vol. 7, pp. 180532–180543, 2019.
[12] Z. Lyu, G. Zhu, and J. Xu, "Joint maneuver and beamforming design for UAV-enabled integrated sensing and communication," *IEEE Trans. Wireless Commun.*, vol. 22, no. 4, pp. 2424–2440, Apr. 2023.

[13] S. Yoon, H. Jung, H. Seo, M. Kang, S. Kim, C.-S. Park, J.-H. Jeon, H.-J. Ju, and S. Kim, "GRPO-based adaptive beamforming for mobility-aware UAV swarm relay systems," *IEEE Access*, vol. 14, pp. 116062–116073, 2026.

[14] B. Dwivedy, S. K. Behera, and V. K. Singh, "A versatile triangular patch array for wideband frequency alteration with concurrent circular polarization and pattern reconfigurability," *IEEE Trans. Antennas Propag.*, vol. 67, no. 3, pp. 1640–1649, Mar. 2019.

[15] B. Dwivedy, "A droplet-shape inspired wideband bow-tie dielectric resonator antenna for sub-6 GHz and IoT applications," *AEU - Int. J. Electron. Commun.*, vol. 178, May 2024, Art. no. 155281.

[16] V. Kabra, N. Kaippalli, V. Joy, and H. Singh, "Low observable Vivaldi antenna array for electronic warfare applications," *Sci. Culture*, vol. 91, pp. 4–11, Jan. 2025.

[17] K. Premchand and P. H. Krishna, "A miniaturized multi-octave Vivaldi antenna for electronic warfare systems," *Electromagnetics*, vol. 40, no. 1, pp. 56–69, Nov. 2019.

[18] I. Kim, H.-Y. Lee, D.-M. Lee, H.-J. Lee, H. Kim, E.-S. Kim, and N.-Y. Kim, "Broadband gain enhanced narrow-beam Vivaldi antenna with ring and directors for handheld antidrone jamming system," *IEEE Antennas Wireless Propag. Lett.*, vol. 23, no. 1, pp. 214–218, Jan. 2024.

[19] F. Abushakra, N. Jeong, A. K. Awasthi, S. Kolpuke, C. Simpson, O. Reyhanigalangashi, D. N. Elluru, A. Bhandari, D. Taylor, and S. P. Gogineni, "Ultra-wideband coplanar Vivaldi antenna array with dielectric patch antenna for grating lobes suppression," *IEEE Access*, vol. 10, pp. 54410–54420, 2022.

[20] M. T. Ozdemiralp, A. S. Turk, and A. Caliskan, "Super wide band parabolic reflector design with Vivaldi antenna array feed for switchable beam applications," *Microw. Opt. Technol. Lett.*, vol. 67, no. 8, pp. 70352–70364, Aug. 2025.

[21] G. Zhao, Y. Xiao, W. Huang, S. Xu, and Z. Chen, "Miniaturized design of Vivaldi antenna based on an improved nonuniform slot profile method for ultrawideband applications," *IEEE Trans. Antennas Propag.*, vol. 73, no. 8, pp. 6199–6204, Aug. 2025.

[22] Y. Zhang and J. Zhang, "Design of a novel ultra-wideband antipodal Vivaldi antenna based on Klopfenstein curve," *Microwave*, vol. 1, no. 4, pp. 1–14, May 2025.

[23] M. Wang, L. Crocco, M. Li, and M. Cavagnaro, "Slot-loaded Vivaldi antenna for biomedical microwave imaging applications: Influence of design parameters on antenna dimensions and performances," *Sensors*, vol. 24, Aug. 2024, Art. no. 5368.

[24] S. Pisa, F. Pastori, R. Cicchetti, E. Piuzzi, O. Testa, E. Pittella, A. Cicchetti, P. D'Atanasio, and A. Zambotti, "An antipodal Vivaldi antenna for a drone-mounted ground probing radar," *Prog. Electromagn. Res. M*, vol. 123, pp. 53–61, 2024.

[25] R. Hu, F. Zhang, S. Ye, and G. Fang, "Ultra-wideband and high-gain Vivaldi antenna with artificial electromagnetic materials," *Micromachines*, vol. 14, no. 7, pp. 1–18, Jun. 2023.

[26] G. Zhao, Y. Xiao, W. Huang, S. Xu, and Z. Chen, "Compact and gain-enhanced Vivaldi antenna design using nonuniform slot profile optimization and aperture dielectric loading," *IEEE Antennas Wireless Propag. Lett.*, vol. 24, no. 7, pp. 1570–1574, Jul. 2025.

[27] J. Liu, C. Xu, H. Yu, and J. Su, "Design of a miniaturized ultrawideband and low scattering antipodal Vivaldi antenna array," *Sci. Rep.*, vol. 11, no. 1, pp. 1–9, Jun. 2021.

[28] D. K. Naik, R. Swain, D. C. Panda, and R. K. Mishra, "CMA approach for a DGS-based wideband circular patch antenna with low cross polarization," *IEEE Antennas Wireless Propag. Lett.*, vol. 22, pp. 586–590, 2023.

[29] N. Supreeyatitikul, P. Janpangngern, T. Lertwiriyaprapa, M. Krairiksh, and C. Phongcharoenpanich, "CMA-based quadruple-cluster leaf-shaped metasurface-based wideband circularly-polarized stacked-patch antenna array for sub-6 GHz 5G applications," *IEEE Access*, vol. 11, pp. 14511–14523, 2023.

[30] N. Sathishkumar, S. Palanisamy, R. Natarajan, K. Ouahada, and H. Hamam, "Design of dual mode antenna using CMA and broadband dual-polarized antenna for 5G networks," *Sci. Rep.*, vol. 14, no. 1, p. 15553, Jul. 2024.

[31] J. Choi, J. Lee, J. Cho, L. Qu, and K.-Y. Jung, "Miniaturization technique for a quasi-Yagi antenna using characteristic mode analysis," *Phys. Scripta*, vol. 100, no. 5, Apr. 2025, Art. no. 055542.

[32] Y. Chen and C.-F. Wang, "Electrically small UAV antenna design using characteristic modes," *IEEE Trans. Antennas Propag.*, vol. 62, no. 2, pp. 535–545, Feb. 2014.

[33] R. Harrington and J. Mautz, "Theory of characteristic modes for conducting bodies," *IEEE Trans. Antennas Propag.*, vol. AP-19, no. 5, pp. 622–628, Sep. 1971.

[34] M.-J. Kang, J. Park, H. Heo, L. Qu, and K.-Y. Jung, "CMA-based design of a novel structure for isolation enhancement and radiation pattern correction in MIMO antennas," *Sci. Rep.*, vol. 15, no. 1, pp. 1–15, Jan. 2025.

[35] H. Heo, M.-J. Kang, S. Park, J. Lee, L. Qu, and K.-Y. Jung, "Design of a UWB circularly-polarized planar monopole antenna using characteristic mode analysis," *Sci. Rep.*, vol. 14, no. 1, pp. 1–15, Oct. 2024.

[36] M.-J. Kang, D. Park, G. Kim, S. Kim, and K.-Y. Jung, "Design of stepped monopole antennas with a novel decoupling structure based on characteristic mode analysis," *Alexandria Eng. J.*, vol. 111, pp. 482–490, Jan. 2025.

[37] W. Chen, C. Liu, W. Wang, M. Peng, and W. Zhang, "Adaptive hybrid beamforming for UAV mmWave communications against asymmetric jitter," *IEEE Trans. Wireless Commun.*, vol. 23, no. 8, pp. 9432–9445, Aug. 2024.

[38] W. Wang and W. Zhang, "Jittering effects analysis and beam training design for UAV millimeter wave communications," *IEEE Trans. Wireless Commun.*, vol. 21, no. 5, pp. 3131–3146, May 2022.

[39] H. Cox, R. M. Zeskind, and M. M. Owen, "Robust adaptive beamforming," *IEEE Trans. Acoust., Speech, Signal Process.*, vol. ASSP-35, no. 10, pp. 1365–1376, Oct. 1987.

[40] K. Deb and H. Jain, "An evolutionary many-objective optimization algorithm using reference-point-based nondominated sorting approach, Part I: Solving problems with box constraints," *IEEE Trans. Evol. Comput.*, vol. 18, no. 4, pp. 577–601, Aug. 2014.

[41] C. A. C. Coello, G. T. Pulido, and M. S. Lechuga, "Handling multiple objectives with particle swarm optimization," *IEEE Trans. Evol. Comput.*, vol. 8, no. 3, pp. 256–279, Jun. 2004.

[42] X. Ma, F. Liu, Y. Qi, X. Wang, L. Li, L. Jiao, M. Yin, and M. Gong, "A multiobjective evolutionary algorithm based on decision variable analyses for multiobjective optimization problems with large-scale variables," *IEEE Trans. Evol. Comput.*, vol. 20, no. 2, pp. 275–298, Apr. 2016.

[43] P. S. Nalumakkal, K. M. Reddy, K. J. Vinoy, and S. Shukla, "Wideband stripline fed tapered slot antenna with integral coupler for wide scan angle active phased array," *IET Microw., Antennas Propag.*, vol. 12, no. 9, pp. 1487–1493, Jul. 2018.

[44] M. Kalfa and E. Halavut, "A fast method for obtaining active S-parameters in large uniform phased array antennas," in *Proc. IEEE Int. Symp. Phased Array Syst. Technol.*, Oct. 2013, pp. 684–688.

[45] M. A. Richards, *Fundamentals of Radar Signal Processing*, vol. 1. New York, NY, USA: McGraw-Hill, 2005.



MYEONG-JUN KANG received the B.S. and integrated M.S./Ph.D. degrees in electronic engineering from Hanyang University, Seoul, Republic of Korea, in 2022 and 2026, respectively. He is currently with Hanwha Systems, Seongnam-si, Gyeonggi-do, South Korea. His research interests include antenna design and analysis, characteristic mode analysis (CMA), ultra-wideband (UWB) antennas, multiple-input multiple-output (MIMO) antenna systems, 5G and 6G upper mid-band antennas, and aircraft-mounted antennas. His current research focuses on developing compact, wideband, and high-performance antenna systems for next-generation wireless communications and aerospace platforms.



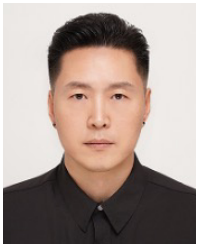
SEONGKWON YOON received the B.S. degree in defense science and technology from Howon University, Gunsan, South Korea, in 2019, and the M.S. and Ph.D. degrees in electronic engineering from Hanyang University, Seoul, South Korea, in 2022 and 2026, respectively. He is currently with the Agency for Defense Development (ADD), Daejeon, South Korea, where he conducts research on intelligence, surveillance, and reconnaissance (ISR) systems. His research interests include digital signal processing, ultra-wideband (UWB) sensing, frequency-modulated continuous wave (FMCW) radar, and distributed beamforming.



JUN-HYEON KANG received the B.S. degree in electronic engineering from Hanyang University, Seoul, South Korea, in 2025, where he is currently pursuing the M.S. degree in electronic engineering. His current research interests include the design and analysis of beam-scanning antennas, phased-array antennas, and reconfigurable antenna systems for wireless communications and radar applications.



SEYEON LEE received the B.S. degree in IT convergence major from the Department of Electronic Information Engineering, Soongsil University, Seoul, South Korea, in 2025. She is currently pursuing the M.S. degree with the Department of Electronic Engineering, Hanyang University, Seoul. Her current research interests include 6G/B6G wireless communication systems, unmanned autonomous vehicle-based communications, beamforming, and positioning systems.



JEAHOON CHO received the B.S. degree in communication engineering from Daejin University, Pocheon, Republic of Korea, in 2004, and the M.S. and Ph.D. degrees in electrical and computer engineering from Hanyang University, Seoul, Republic of Korea, in 2006 and 2015, respectively. From 2015 to August 2016, he was a Postdoctoral Researcher with Hanyang University. Since September 2016, he has been with Hanyang University, where he is currently a Research Professor. His current research interests include computational electromagnetics and EMP/EMI/EMC analysis.



SUNWOO KIM (Senior Member, IEEE) received the B.S. degree from Hanyang University, Seoul, South Korea, in 1999, and the Ph.D. degree from the Department of Electrical and Computer Engineering, University of California, Santa Barbara, in 2005. He was the Director of the 5G/Unmanned Vehicle Research Center, funded by the Ministry of Science and ICT, South Korea. Since 2005, he has been with the Department of Electronic Engineering, Hanyang University, where he is currently a Professor and the Department Chair. He is also the Director of the Beyond-G Global Innovation Center. He is also a frequent visitor to the Laboratory for Information and Decision Systems, Massachusetts Institute of Technology. His research interests include wireless communications, sensing, and localization. He served as an Associate Editor for IEEE TRANSACTIONS ON VEHICULAR TECHNOLOGY.